Acta Astronautica 72 (2012) 165–177

Contents lists available at SciVerse ScienceDirect

Acta Astronautica

journal homepage: www.elsevier.com/locate/actaastro

Precise modelling of solar and thermal accelerations on Rosetta ☆

Takahiro Kato [a,*], Jozef C. van der Ha [b]

[a] Kyushu University, Japan
[b] Mission Design and Operations, USA

ARTICLE INFO

Article history:
Received 8 February 2011
Received in revised form
24 August 2011
Accepted 17 September 2011
Available online 17 November 2011

Keywords:
Rosetta
Solar radiation pressure
Thermal effect
Orbit determination

ABSTRACT

This paper presents an analytical approach for the high-fidelity model of the accelerations induced by the Solar Radiation Pressure (SRP) and the Thermal Recoil Pressure (TRP) on ESA's Rosetta spacecraft. The relevant gravitational forces that are induced by planets, moons, and asteroids can readily be incorporated for predicting interplanetary trajectories. However, there are additional perturbation forces that cause residual errors in the orbit determination process. These are the so-called "small forces", which are mainly induced by the SRP and TRP effects and are often not modelled adequately or not completely. In the case of deep-space missions, the spacecraft travels a wide range of distances relative to the Sun. This makes the spacecraft exposed to a wide range of solar fluxes and surface temperatures. This paper establishes a high-fidelity acceleration model, which enables more precise orbit predictions for interplanetary spacecraft. The application of the model is demonstrated and validated using the orbit determination data and in-flight temperature data of the Rosetta spacecraft.

1. Introduction

The navigation of a deep-space spacecraft requires precise models of all forces affecting the orbital motion. The relevant gravitational forces that are induced by planets, moons, and asteroids can readily be incorporated for predicting interplanetary trajectories. However, there are additional perturbation forces that cause a residual error in the orbit determination process. These are the so-called "small forces" that are mainly induced by Solar Radiation Pressure (SRP) and Thermal Recoil Pressure (TRP). In many applications, these forces are corrected by means of scale factors that are estimated from the observed residuals produced by the orbit determination process.

On deep-space trajectories, the spacecraft travels a wide range of distances relative to the Sun. This exposes the spacecraft to a wide range of solar fluxes and surface temperatures. Therefore, in addition to SRP accelerations, TRP effects on the relevant surfaces, i.e. solar arrays and spacecraft body, may induce another significant source of perturbing accelerations on deep-space trajectories.

The motivation for the present research originated from the anomalous accelerations observed during the first Earth swing-by of ESA's Rosetta spacecraft [1]. Although it did not resolve the elusive swing-by anomaly, a previous study [2] showed that the acceleration induced by TRP has an appreciable effect on Rosetta's orbit.

During Rosetta's 6-year operations phase, acceleration errors in the order of 5% to 10% of the SRP magnitude were observed during the heliocentric cruise phase [3]. This paper investigates the origins of the residual errors between the predicted and the measured trajectories of Rosetta.

There are many papers dealing with the modelling of non-conservative forces on satellite missions [4,5]. Based on the knowledge in these previous papers, we follow an analytical method for modelling the SRP and TRP effects in a step-by-step approach to acquire specific insights on the accelerations exerted on deep-space spacecraft.

☆ This paper was presented during the 61st IAC in Prague.

* Corresponding author. Tel.: +81 92 531 8374.
E-mail addresses: takahiro@aero.kyushu-u.ac.jp, takahiro117@gmail.com (T. Kato), jvdha@aol.com (J.C. van der Ha).

0094-5765/$ - see front matter © 2011 Elsevier Ltd. All rights reserved.
doi:10.1016/j.actaastro.2011.09.009

Our approach can be divided into two parts. One is the SRP acceleration model, which includes the effect due to the High Gain Antenna (HGA). The other is the TRP acceleration model derived from the straightforward heat balances and analytical temperature calculations. Furthermore, actual in-flight HGA pointing histories and solar array temperature measurements were taken into account.

So far, the orbit determination software of the European Space Operations Centre (ESOC) does not include a TRP model. In order to account for the observed OD residuals, ESOC uses scale factors in their SRP models. In routine operations, the main scale factor component along the Sun-spacecraft direction is estimated whereas the other two components are treated as 'consider' parameters. The present study aims at the establishment of analytical SRP and TRP acceleration models to enhance the operational orbit determination and prediction accuracy of deep-space trajectories.

2. Spacecraft Rosetta

2.1. Mission of Rosetta

The main milestones of the Rosetta mission are summarized in Table 1. On 10th of July, 2010, Rosetta successfully performed a fly-by of the Lutetia asteroid. At the time of writing, the satellite is getting ready for its almost 3-years long hibernation phase toward the next target of the mission.

An issue that must be kept in mind is the enormous range in solar distance that deep-space missions have to cope with. In the case of Rosetta, the trajectory extends from about 0.9 AU up to 5.3 AU.

A consequence of the wide range of solar distance is that the incident solar power received by the spacecraft is even wider because it varies with the inverse-square of the distance from the Sun. Therefore, Rosetta has two huge Solar Array Panels (SAPs) of over 32 m^2 each that are able to operate at about 5 AU in deep space, see Fig. 1.

2.2. Spacecraft properties

The dimensions of the Rosetta spacecraft and the thermal-optical properties of the relevant surfaces are summarized in Tables 2 and 3, respectively. Since we study the SRP and TRP effects, we mainly focus on the SAPs, the $+X$ and $+Z$ sides of the spacecraft body, and the HGA because these are the surface elements that are subjected to direct sunlight throughout the mission of Rosetta.

Table 1
Main mission milestones of Rosetta.

Events	Dates [DD/MM/YY]
Launch	02/03/04
Earth swing-by	04/03/05, 13/11/07, 13/11/09
Mars swing-by	25/07/07
Asteroid fly-bys	Steins: 05/09/08 Lutetia: 10/07/10
Hibernation phase	2011–2014
Comet rendezvous	22/05/14

Fig. 1. Illustration of Rosetta during Earth swing-by.

Table 2
Features of Rosetta spacecraft.

Representative mass [kg]	3000
Dimensions	
SAPs: A_{SAP} [m^2]	64.62
Body$+X$ side: A_{+X} [m^2]	5.15
Body$+Z$ side: A_{+Z} [m^2]	4.20
HGA radius : R [m]	1.1
HGA depth [m]	0.344

Table 3
Thermal-optical properties of Rosetta surfaces.

Body MLI surfaces	
Absorptivity, α_{MLI}	0.93
Emissivity, ε_{MLI}	0.86
Specular reflectivity, $\rho_{s,MLI}$	0
Diffuse reflectivity, $\rho_{d,MLI}$	0.07
SAPs	
Absorptivity, α_{SAP}	0.843
Emissivity of front side, ε_f	0.783
Specular reflectivity, $\rho_{s,SAP}$	0.141
Diffuse reflectivity, $\rho_{d,SAP}$	0.016
HGA	
Absorptivity, α_{HGA}	0.93
Specular reflectivity, $\rho_{s,HGA}$	0.01
Diffuse reflectivity, $\rho_{d,HGA}$	0.06

The emissivity of the SAPs' rear sides is known from on-ground experiments [6,7] as a function of the rear side surface temperature T_r (in [K]) as

$$\varepsilon_r(T_r) = 0.312 + 3.288 \times 10^{-3} T_r - 5.33 \times 10^{-6} T_r^2 \quad (1)$$

In addition, we note that the analytical approach established in this paper is specifically applied to Rosetta's cruise phases. Therefore, the following conditions are essentially always satisfied with good accuracy [6]:

- Sun is kept within the $+X$, $+Z$ quadrant of the spacecraft body frame.
- SAPs are always facing normal to the Sun direction.

Since we focus on the heliocentric cruise phases of the mission, we consider the intervals listed in Table 4.

Table 4
Cruise phases of Rosetta.

Phase	Start [YY/MM/DD]	End [YY/MM/DD]	Days
Cruise 1	04/06/07	04/09/05	91
Cruise 2	05/04/05	06/07/28	480
Cruise 3	07/05/29	07/09/12	107
Cruise 4	08/01/28	08/08/03	189
Cruise 5	08/10/06	09/09/13	343

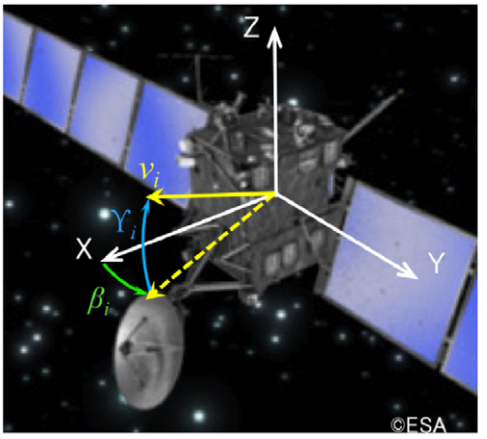

Fig. 2. Local reference frame and notations.

3. Notations

3.1. Local reference frame and angles

For the establishment of the precise analytical acceleration model, we need to define the geometry of each relevant spacecraft surface and to introduce a suitable local reference frames. Fig. 2 shows the definitions of the mechanical frame $\boldsymbol{F_m}$ and the notation angles used in this study. Using the coordinates and notations introduced here, we can establish the unit normal vectors of the respective satellite surface elements and the Sun vector in $\boldsymbol{F_m}$.

The inertial orientations of the $\boldsymbol{F_m}$ axes are given by the attitude data provided by ESOC Toolkit for Auxiliary Science Calculations (TASC) website [8] in terms of quaternions, i.e. $\boldsymbol{q}=[q_1\ q_2\ q_3\ q_4]^T$. Therefore, the rotation matrix R^{mi} from the inertial frame to the mechanical frame can be expressed as

$$R^{mi}=\begin{bmatrix} q_1^2-q_2^2-q_3^2+q_4^2 & 2(q_1q_2+q_3q_4) & 2(q_1q_3-q_2q_4) \\ 2(q_1q_2-q_3q_4) & -q_1^2+q_2^2-q_3^2+q_4^2 & 2(q_2q_3+q_1q_4) \\ 2(q_1q_3+q_2q_4) & 2(q_2q_3-q_1q_4) & -q_1^2-q_2^2+q_3^2+q_4^2 \end{bmatrix} \tag{2}$$

When taking $\boldsymbol{F_m}$ as the main local reference frame, the pointing motions of the SAPs and HGA can be described in terms of the elevation and azimuth angles with respect to $\boldsymbol{F_m}$. These angles are defined as;

- Azimuth β: positive rotation along $+Z$ axis
- Elevation γ: positive rotation along $-Y$ axis

The pointing orientations of the HGA and SAPs are expressed using the elevation and azimuth angles shown in Fig. 2.

In the special case of Rosetta, the spacecraft attitude is controlled such that the unit Sun vector $\mathbf{s}$ is kept within the $+X$, $+Z$ quadrant of $\boldsymbol{F_m}$. Therefore, the Sun vector in $\boldsymbol{F_m}$ can be expressed by means of its elevation angle γ_s

$$\mathbf{s}=\begin{bmatrix} C_{\gamma s} \\ 0 \\ S_{\gamma s} \end{bmatrix} \tag{3}$$

The rotation matrix from $\boldsymbol{F_h}$ to $\boldsymbol{F_m}$, i.e. R^{mh}, can be expressed in terms of the HGA elevation and azimuth angles γ_h and β_h, respectively, as follows:

$$R^{mh}=\begin{bmatrix} C_{\gamma h}C_{\beta h} & -C_{\gamma h}S_{\beta h} & -S_{\gamma h} \\ S_{\beta h} & C_{\beta h} & 0 \\ S_{\gamma h}C_{\beta h} & S_{\gamma h}S_{\beta h} & C_{\gamma h} \end{bmatrix} \tag{4}$$

where C_i and S_i are the cosine and sine of the angle i, respectively.

Fig. 3 shows the local coordinate frame of the HGA (h_1, h_2, h_3). The h_1 axis represents the HGA pointing direction and the HGA pointing angles are defined by using the angle between the h_1 axis and spacecraft mechanical frame $\boldsymbol{F_m}$. To express an arbitrary surface normal $\mathbf{n}_{HGA}$ vector on the HGA dish inner surface in the presence of its curvature, we introduce the local notations shown in Fig. 3, see also [9].

When utilizing the coordinate frame shown in Fig. 3, we can express an arbitrary unit-length surface normal vector as

$$\mathbf{n}_{HGA}=\begin{bmatrix} C_\eta \\ -S_\eta C_\varphi \\ -S_\eta S_\varphi \end{bmatrix} \tag{5}$$

Next, we calculate the angle η from the HGA height h and radius R

$$\tan\eta \approx \frac{2hr}{R^2}=2up \tag{6}$$

where u is a constant and p is a geometrical variable defined as

$$u=\frac{h}{R},\quad p=\frac{r}{R} \tag{7a, b}$$

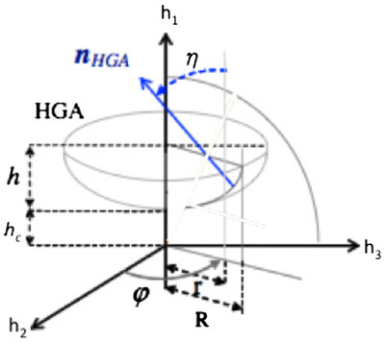

Fig. 3. HGA local coordinate.

so that

$$\cos\eta = \frac{1}{\sqrt{1+4u^2p^2}}, \quad \sin\eta = \frac{2up}{\sqrt{1+4u^2p^2}} \tag{8a, b}$$

Finally, we have

$$\mathbf{n}_{HGA} = \frac{1}{\sqrt{1+4u^2p^2}} \begin{bmatrix} 1 \\ -2upC_\varphi \\ -2upS_\varphi \end{bmatrix} \tag{9}$$

3.2. HGA pointing model

In order to calculate the SRP acceleration components on the HGA analytically, we process the HGA data to eliminate the spikes in its pointing history.

First, we allocate the HGA pointing angle data to each specific cruise phase interval. Then, the motion of the HGA is modelled according to the actual elevation and azimuth angles contained in the telemetry data.

Fig. 4 shows the raw HGA elevation and azimuth data during cruise 1. The horizontal axis shows the date in [YY/MM/DD], and the measured angular data are shown in degrees.

From these measurement data in Fig. 4, we model the HGA motion as shown in Fig. 5.

The HGA pointing angles in the other cruise phases are modelled in the same manner. The following Figs. 6–10 show the modelled HGA elevation and azimuth angles together with the elevation of the Sun in each cruise phase. We note that angles are expressed in $\boldsymbol{F_m}$ as defined in Fig. 2.

The spikes in the Sun elevations that are shown in Figs. 6–10 are due to the spacecraft attitude motion. There are spacecraft attitudes and Sun–spacecraft–Earth geometries that deviate from the nominal smooth attitude pointing motion (i.e. the HGA kept in Earth pointing mode). These violations are introduced because of the testing and commissioning requirements of on-board instruments. The HGA pointing models and the evolutions of the Sun shown in Figs. 6–10 are implemented in the calculations of the acceleration components.

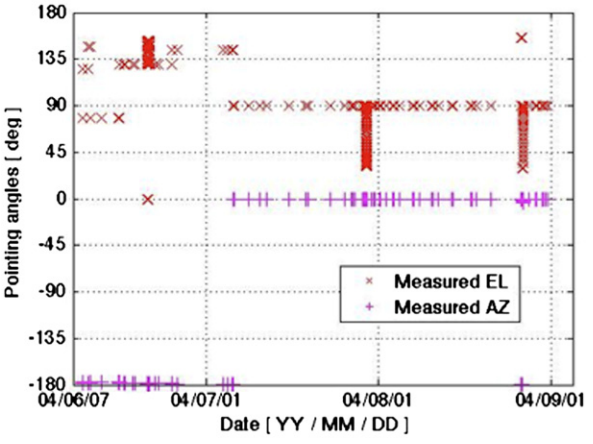

Fig. 4. Measured HGA pointing angles in cruise 1.

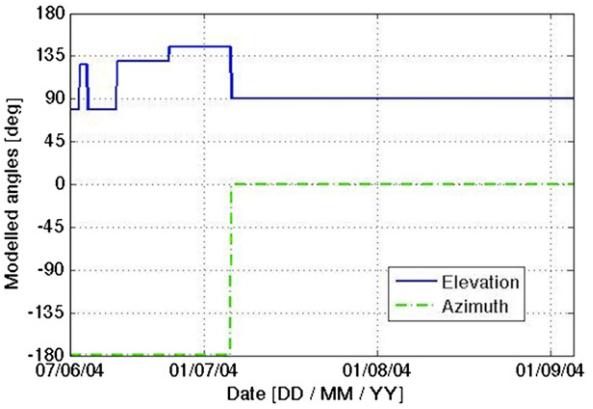

Fig. 5. HGA pointing model in cruise 1.

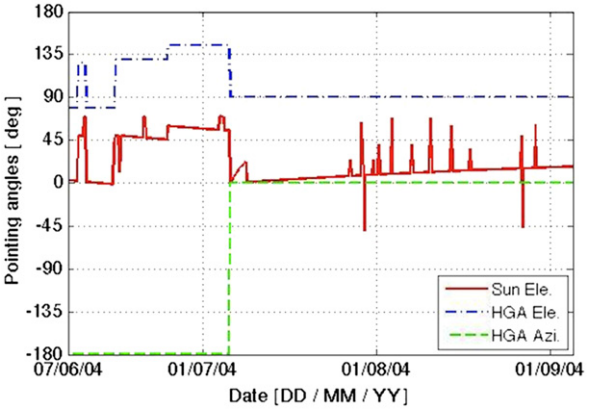

Fig. 6. Sun and HGA pointing angles in cruise 1.

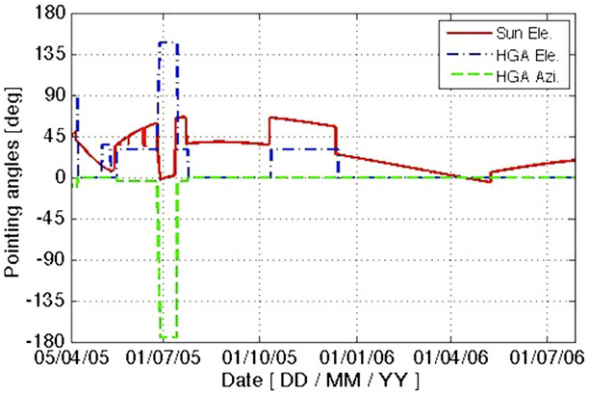

Fig. 7. Sun and HGA pointing angles in cruise 2.

4. Acceleration models

4.1. SRP acceleration model

Fig. 11 (a)–(c) shows general interactions of the incident sunlight on a flat surface. The incoming solar radiation is either absorbed or reflected by the surface. In addition, there are two different types of reflections, i.e. specular and diffuse reflections.

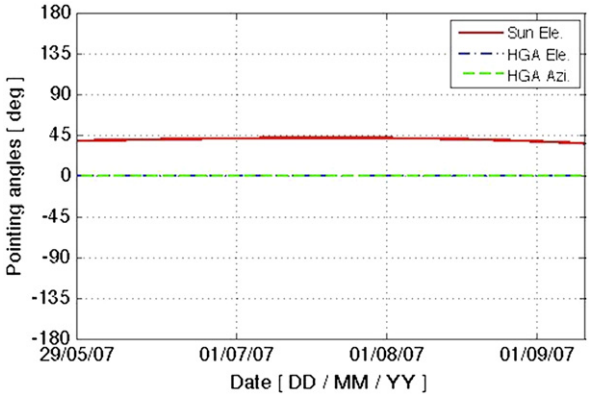

Fig. 8. Sun and HGA pointing angles in cruise 3.

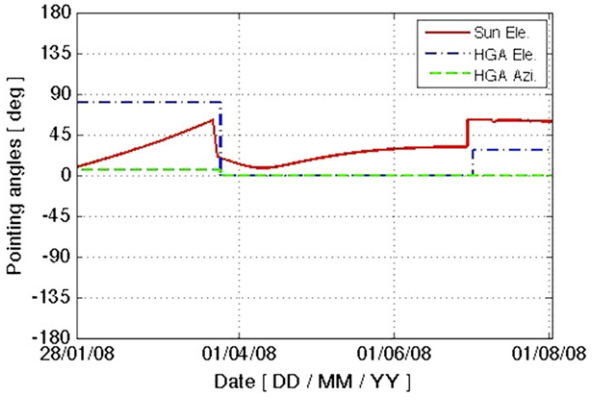

Fig. 9. Sun and HGA pointing angles in cruise 4.

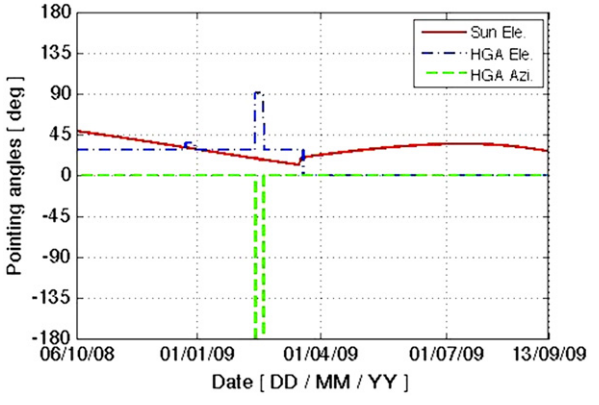

Fig. 10. Sun and HGA pointing angles in cruise 5.

The characteristics of the interactions are determined by the optical properties of the surface. They are expressed by the absorptivity α, the specular reflectivity ρ_s, and the diffuse reflectivity ρ_d. Each of these interactions can be formulated in terms of these optical properties as

$$\mathbf{a}_{abs} = -\alpha c_{SRP} A |\mathbf{n}\cdot\mathbf{s}| \mathbf{s} \tag{10}$$

$$\mathbf{a}_{spe} = -2\rho_s c_{SRP} A |\mathbf{n}\cdot\mathbf{s}| (\mathbf{n}\cdot\mathbf{s})\mathbf{s} \tag{11}$$

$$\mathbf{a}_{diff} = -\rho_d c_{SRP} A |\mathbf{n}\cdot\mathbf{s}| \left(\mathbf{s}+\tfrac{2}{3}\mathbf{n}\right) \tag{12}$$

Here, the notation of $|\mathbf{n}\cdot\mathbf{s}|$ represents the absolute value of the dot product. We assume that the diffuse reflection follows Lambert's cosine law and this introduces the factor 2/3 in Eq. (12). The c_{SRP} term is the coefficient of the acceleration induced by the solar radiation based on the mass m, the speed of light c, and the solar flux q_{1AU} at 1 AU as follows:

$$c_{SRP}(r) = \frac{q_{1AU}}{mc}\left(\frac{R_0}{r}\right)^2 \left[\mathrm{m/s^2}\right] \tag{13}$$

where R_0 is the Sun–Earth distance and r is the distance of Rosetta from the Sun. In addition, mass history data at each point of time are also taken into account.

By considering the flat surface in Fig. 11 as a small element of a large surface area such as the SAPs or HGA, we can obtain the acceleration components by integrating over the total surface area. As a consequence, the total acceleration acting on the spacecraft can be expressed as the sum of the acceleration produced by the surface elements of the SAPs, $+X$, $+Z$, and HGA as

$$\mathbf{a}_{SRP} = -c_{SRP}(r)\sum_{i=1}^{4}\iint_{A_i} |\mathbf{n}_i\cdot\mathbf{s}| \times \left\{(\alpha_i+\rho_{d,i})\mathbf{s} + \left[\frac{2}{3}\rho_{d,i} + 2\rho_{s,i}(\mathbf{n}_i\cdot\mathbf{s})\right]\mathbf{n}_i\right\} dA_i \tag{14}$$

Using the surface normal vectors expressed in the mechanical frame $\boldsymbol{F_m}$, we obtain the acceleration components expressed in $\boldsymbol{F_m}$.

4.1.1. SRP on SAPs

For the SAPs, the unit normal vector on the surface $\mathbf{n}_{SAP}$ is identical to the Sun vector for Rosetta's situation, so we have

$$\mathbf{n}_{SAP}\cdot\mathbf{s} = 1 \tag{15}$$

When substituting the Sun vector $\mathbf{s}$ instead of $\mathbf{n}$ in Eq. (14), we obtain the SRP acceleration vector due to the SAPs as

$$\mathbf{a}_{SRP,SAP} = -c_{SRP}(r)A_{SAP}\begin{bmatrix}(\alpha_1+\frac{5}{3}\rho_{d,1}+2\rho_{s,1})C_{\gamma s}\\ 0\\ (\alpha_1+\frac{5}{3}\rho_{d,1}+2\rho_{s,1})S_{\gamma s}\end{bmatrix} \tag{16}$$

4.1.2. SRP on $+X$ side

The SRP acceleration components on the $+X$ surface can be obtained using the unit vector $\mathbf{n}_{+X}=[1\ 0\ 0]^T$ along the x-axis of $\boldsymbol{F_m}$ as follows:

$$\mathbf{n}_{+X}\cdot\mathbf{s} = C_{\gamma s} \tag{17}$$

$$\mathbf{a}_{SRP,+X} = -c_{SRP}(r)A_{+X}|C_{\gamma s}| \times \begin{bmatrix}(\alpha_2+\rho_{d,2}+2\rho_{s,2})C_{\gamma s}+\frac{2}{3}\rho_{d,2}\\ 0\\ (\alpha_2+\rho_{d,2})S_{\gamma s}\end{bmatrix} \tag{18}$$

4.1.3. SRP on $+Z$ side

The acceleration components on the $+Z$ surface can be obtained in the same manner as done in Section 4.1.2

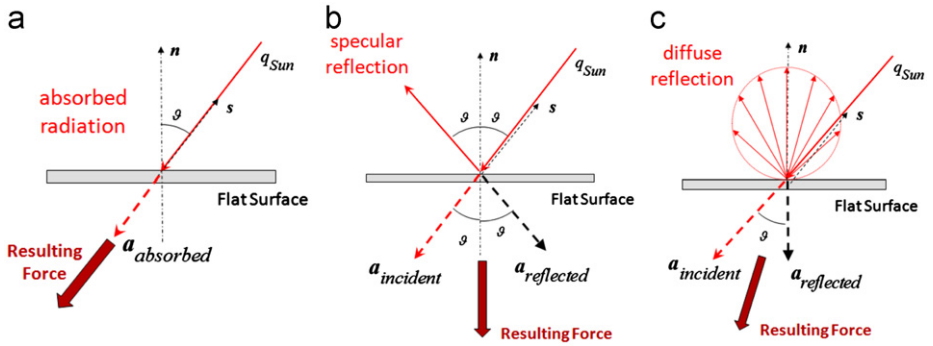

Fig. 11. Solar radiation interactions on flat surface. (a) Absorption; (b) Specular reflection; (c) Diffuse reflection.

using the unit vector $\mathbf{n}_{+Z}=[0\ 0\ 1]^T$ along the z-axis of $\boldsymbol{F_m}$

$$\mathbf{n}_{+Z}\cdot\mathbf{s}=S_{\gamma s} \tag{19}$$

$$\mathbf{a}_{SRP,+Z}=-c_{SRP}(r)A_{+Z}|S_{\gamma s}| \times\begin{bmatrix}(\alpha_3+\rho_{d,3})C_{\gamma s}\\0\\(\alpha_3+\rho_{d,3}+2\rho_{s,3})S_{\gamma s}+\frac{2}{3}\rho_{d,3}\end{bmatrix} \tag{20}$$

4.1.4. SRP on HGA

From the R^{mh} and Eq. (9), the unit surface normal on the HGA in $\boldsymbol{F_m}$ can be expressed as

$$\mathbf{n}_{HGA,m}=R^{mh}\mathbf{n}_{HGA} \tag{21}$$

From Eq. (9), it is clear that the dot product between the normal $\mathbf{n}_{HGA,m}$ and the Sun vector $\mathbf{s}$ contains p and φ, which are variables in the areal integral. Therefore, we cannot obtain the analytical solution from Eq. (14). Thus, we analyze the case by using the dot product of the unit vector h_1 (i.e. along the h_1-axis of the HGA local frame) and the Sun vector $\mathbf{s}$ instead of $\mathbf{n}_{HGA,m}\cdot\mathbf{s}$ to determine the sign of the absolute value of $\mathbf{n}_{HGA,m}\cdot\mathbf{s}$

Case 1 $h_1\cdot s\geq 0$ $\quad|\mathbf{n}_{HGA,m}\cdot\mathbf{s}|=\mathbf{n}_{HGA,m}\cdot\mathbf{s}$
Case 2 $h_1\cdot s<0$ $\quad|\mathbf{n}_{HGA,m}\cdot\mathbf{s}|=-(\mathbf{n}_{HGA,m}\cdot\mathbf{s})$

Physically, in Case 1, the front surface of the HGA is illuminated and, in Case 2, the rear side is illuminated. Since the dish of the HGA is not flat (we note that the maximum of η is about 32 deg), there are intervals when the HGA is partially illuminated. However, judging the illumination by the straightforward criterion $h_1\cdot s$ is the most practical approach since the present analytical model does not include the partially illuminated condition. Under the Case 1 condition, we obtain

$$\mathbf{a}_{SRP,\ HGA}=-\pi R^2 c_{SRP}(r) \times\begin{bmatrix}(\alpha_4+\rho_{d,4})K_1+\rho_{d,4}(K_2I_1+K_3I_2)+\rho_{s,4}(K_4I_3+K_5I_4)\\\rho_{d,4}(K_6I_1+K_7I_2)+\rho_{s,4}(K_8I_3+K_9I_4)\\(\alpha_4+\rho_{d,4})K_{10}+\rho_{d,4}(K_{11}I_1+K_{12}I_2)+\rho_{s,4}(K_{13}I_3+K_{14}I_4)\end{bmatrix} \tag{22}$$

where K_i $(i=1,2,\ldots,14)$ are constants defined by the pointing angles of the Sun and the HGA at each point of time, and I_j $(j=1, 2, 3, 4)$ are constants determined by the geometrical constant u in Eq. (7). They are expressed as follows:

$$K_1=C_{\gamma s}C_{\beta h}C_{(\gamma s-\gamma h)} \tag{23}$$

$$K_2=C_{\gamma h}C_{\beta h}^2C_{(\gamma s-\gamma h)} \tag{24}$$

$$K_3=2(C_{\gamma h}S_{\beta h}^2C_{(\gamma s+\gamma h)}+S_{\gamma h}S_{(\gamma h-\gamma s)}) \tag{25}$$

$$K_4=C_{\gamma h}C_{\beta h}^3C_{(\gamma s-\gamma h)}^2 \tag{26}$$

$$K_5=C_{\gamma h}C_{\beta h}(S_{\beta h}^2C_{(\gamma s+\gamma h)}^2+S_{(\gamma h-\gamma s)}^2)+C_{\beta h}C_{(\gamma s-\gamma h)}K_3 \tag{27}$$

$$K_6=S_{\beta h}C_{\beta h}C_{(\gamma s-\gamma h)} \tag{28}$$

$$K_7=-2S_{\beta h}C_{\beta h}C_{(\gamma s+\gamma h)} \tag{29}$$

$$K_8=S_{\beta h}C_{\beta h}^2C_{(\gamma s-\gamma h)}^2 \tag{30}$$

$$K_9=S_{\beta h}(S_{\beta h}^2C_{(\gamma s+\gamma h)}^2+S_{(\gamma h-\gamma s)}^2)+C_{\beta h}C_{(\gamma s-\gamma h)}K_7 \tag{31}$$

$$K_{10}=S_{\gamma s}C_{\beta h}C_{(\gamma s-\gamma h)} \tag{32}$$

$$K_{11}=S_{\gamma h}C_{\beta h}^2C_{(\gamma s-\gamma h)} \tag{33}$$

$$K_{12}=-2(S_{\gamma h}S_{\beta h}^2C_{(\gamma s+\gamma h)}+C_{\gamma h}S_{(\gamma h-\gamma s)}) \tag{34}$$

$$K_{13}=S_{\gamma h}C_{\beta h}^3C_{(\gamma s-\gamma h)}^2 \tag{35}$$

$$K_{14}=S_{\gamma h}C_{\beta h}(S_{\beta h}^2C_{(\gamma s+\gamma h)}^2+S_{(\gamma h-\gamma s)}^2)+C_{\beta h}C_{(\gamma s-\gamma h)}K_3 \tag{36}$$

$$I_1=\frac{\sqrt{1+4u^2}-1}{3u^2} \tag{37}$$

$$I_2=\frac{2}{3}\left\{2\sqrt{1+4u^2}-\frac{(1+4u^2)^{3/2}-1}{6u^2}\right\} \tag{38}$$

$$I_3=\frac{\log(1+4u^2)}{2u^2} \tag{39}$$

$$I_4=\frac{4u^2-\log(1+4u^2)}{4u^2} \tag{40}$$

For Case 2, we simply change the sign of Eq. (22).

4.2. TRP acceleration model

This section explains the simplified heat balances for each surface element. As an analytical model, the heat balances considered here are based on one-dimensional relationships between the incoming and outgoing heat fluxes on each of the four surface elements. We calculate the temperatures for each surface, which determine the TRP acceleration magnitude.

4.2.1. Heat balance on SAP surface

Fig. 12 shows the heat balance of the SAPs with different front and rear temperatures. The unit vectors ***lmn*** represent the local coordinate axes on the SAPs in general. For Rosetta's case, we assume that the SAPs are always pointing to the Sun. Therefore, the unit vector **l** can be replaced by the Sun vector **s**.

The emitted heat fluxes from the front and rear SAP surfaces $q_{f,out}$ and $q_{r,out}$ are functions of the surface temperatures T_f and T_r, respectively. With the help of the respective front and rear emissivities, we find using Stephan–Boltzmann's law [4]

$$q_{f,out} = \varepsilon_f \sigma T_f^4, \quad q_{r,out} = \varepsilon_r \sigma T_r^4 \tag{41}$$

with Stephan–Boltzmann constant defined as $\sigma = 5.67 \times 10^{-8}$ [W/(m^{2}K^4)]. The absorbed portion of the incoming solar heat flux is denoted as q_{in} in Fig. 12. The heat flux absorbed by the SAP surfaces is expressed in terms of its absorptivity α as

$$q_{in,SAP}(r) = \alpha_{SAP} \frac{q_{1\,\mathrm{AU}}}{r^2} \tag{42}$$

where $q_{1\ \mathrm{AU}}$ is the solar flux at 1 AU that is 1367 [W/m^2]. The parameter r is the distance from the Sun at each point of time. We can develop the analytical heat balance relationship by assuming no heat losses inside the SAP core

$$q_{in,SAP} = q_{f,out} + q_{r,out} \tag{43}$$

The emissivity of the rear panel is given in Eq. (1), therefore, Eq. (43) can be written as an equation in terms of T_r

$$\varepsilon_r(T_r)\sigma T_r^4 = q_{in,SAP}(r) - \varepsilon_f \sigma T_f^4 \tag{44}$$

Since we have the measurement data of T_f [7], the resulting equation is a 6th degree polynomial in T_r. The unknown temperature T_r can be obtained as a root of the polynomial. We select the root, which is a real number and is smaller than T_f. This procedure has worked smoothly in all cases considered.

4.2.2. Heat balances on X surfaces

Based on the assumption that the whole spacecraft body is covered with MLI, we can analytically obtain the temperature of the body surface using the thermal-optical properties of MLI. The basic assumption for the analytical model is that the model uses the one-dimensional heat balance while neglecting the small heat exchanges between one surface and the other body surfaces, see Fig. 13.

We have the net amount of solar heat input on the $+X$ surface as follows:

$$q_{in,+X} = q_{in} \cos\gamma_s \tag{45}$$

The heat flux through the MLI from the inside of the satellite is given as $q_{MLI} = 5$ [W/m^2] [6]. Therefore, we have the heat balance equation

$$q_{in,+X} = q_{+X,out} + q_{MLI} \tag{46}$$

or

$$T_{+X} = \left\{ \frac{1}{\varepsilon_{MLI}\sigma} (q_{in,+X} - q_{MLI}) \right\}^{1/4} \tag{47}$$

On the other hand, for the $-X$ surface, all of the heat flux coming through the MLI from inside the satellite is emitted. Thus, we have

$$T_{-X} = \left(\frac{q_{MLI}}{\varepsilon_{MLI}\sigma} \right)^{1/4} \tag{48}$$

4.2.3. Heat balances on Z surfaces

In the same manner as the X surfaces, we can develop the heat balance equations in $+Z/-Z$ surfaces, see Fig. 14

$$q_{in,+Z} = q_{in} \sin\gamma_s \tag{49}$$

$$q_{in,+Z} = q_{+Z,out} + q_{MLI} \tag{50}$$

thus, we obtain

$$T_{+Z} = \left\{ \frac{1}{\varepsilon_{MLI}\sigma} (q_{in,+Z} - q_{MLI}) \right\}^{1/4} \tag{51}$$

$$T_{-Z} = \left(\frac{q_{MLI}}{\varepsilon_{MLI}\sigma} \right)^{1/4} \tag{52}$$

Using this approach, the temperatures of the $-X$ and the $-Z$ surfaces are always at the same temperature of -172.5 [°C]. This result is adequate under the assumption

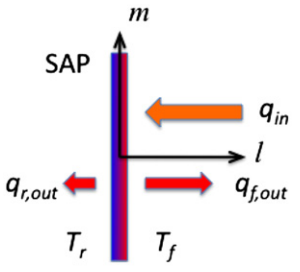

Fig. 12. Heat balance on the SAP front and rear side.

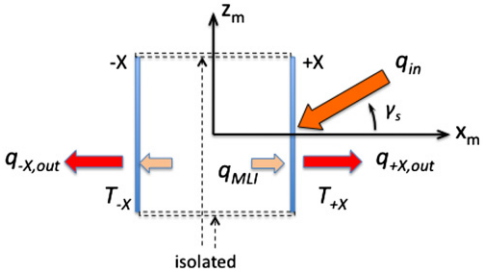

Fig. 13. Heat balance of $+X/-X$ surfaces.

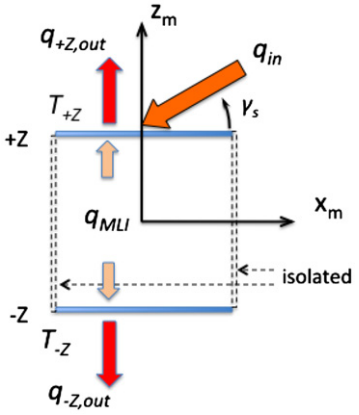

Fig. 14. Heat balance of $+Z/-Z$ panels.

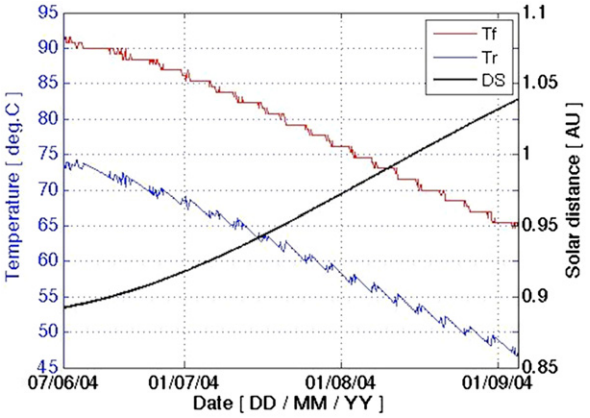

Fig. 15. Front and rear temperatures of the SAPs and solar distance in cruise 1.

that these two side surfaces are always kept in the shadow.

There are 3 thermistors attached to the front surface of the SAPs. Each SAP contains five sub-panels and two of the thermistors are placed at the two sub-panels nearest to the spacecraft body and the third one is placed at the outermost sub-panel [7]. We use the average temperature of the two outer thermistors on each of the SAPs as the temperature input for T_f.

Figs. 15–19 show the temperatures T_f and T_r of the front and rear side of the SAPs, respectively, together with the distance of the Sun (SD) in each cruise phase. The red line is the measured temperature of the SAPs front surface and the blue line is the calculated rear surface temperature from the heat balance in Eq. (44).

The calculated results using the proposed analytical approach presented here are practically identical to those of the numerical finite element method used in Ref. [7].

4.3. Analytical TRP acceleration model

Using the established analytical heat balance equations, we obtain the TRP acceleration components on each of the relevant surfaces.

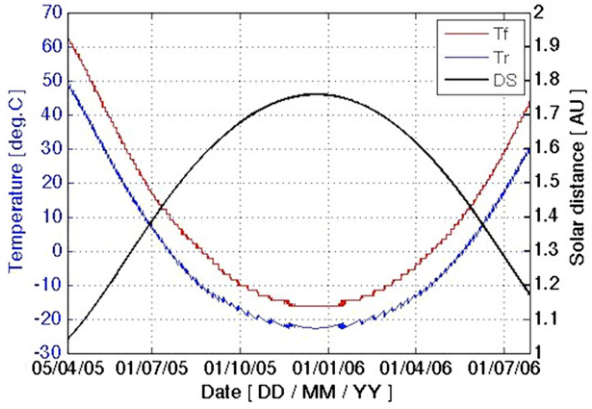

Fig. 16. Front and rear temperatures of the SAPs and solar distance in cruise 2.

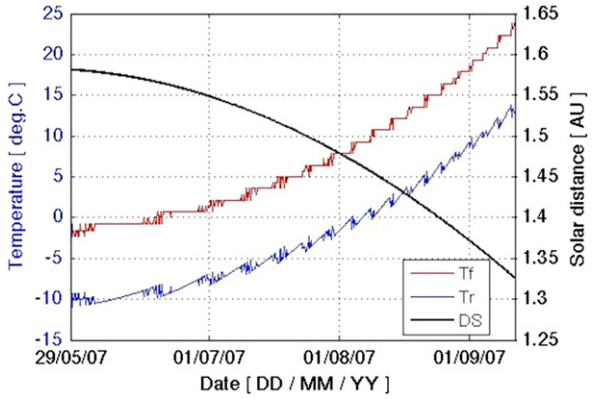

Fig. 17. Front and rear temperatures of the SAPs and solar distance in cruise 3.

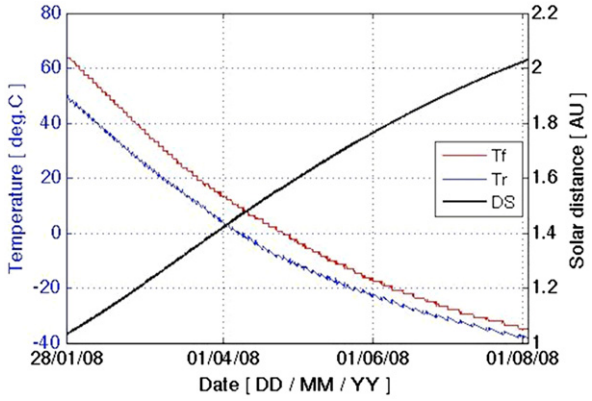

Fig. 18. Front and rear temperatures of the SAPs and solar distance in cruise 4.

Assuming that the thermal emission follows Lambert's cosine law as shown in Fig. 11(c), the thermal recoil pressure force F_{TRP} due to the emission over the surface A_i can be obtained, using the speed of light c [4]

$$F_{TRP,i} = \frac{2}{3}\frac{q_{net,i}}{c}A_i \tag{53}$$

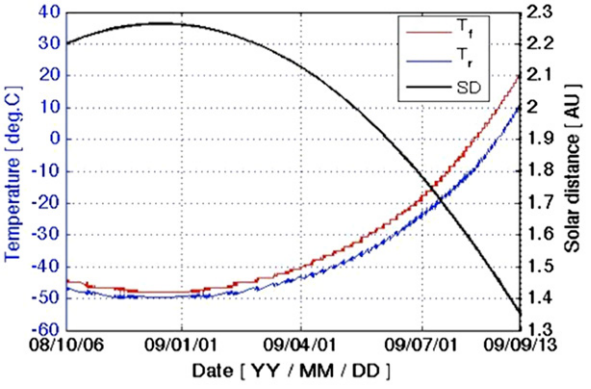

Fig. 19. Front and rear temperatures of the SAPs and solar distance in cruise 5.

Here $q_{net,i}$ is the net heat flux used for the TRP acceleration of each surface i. Therefore, the TRP acceleration vector is expressed as

$$\mathbf{a}_{TRP} = -\sum_i \frac{F_{TRP,i}}{m}\mathbf{n}_i \tag{54}$$

The net heat fluxes for each surface are as follows:

$$q_{net,SAP} = q_{f,out} - q_{r,out} \tag{55}$$

$$q_{net,X} = q_{+X,out} - q_{-X,out} \tag{56}$$

$$q_{net,Z} = q_{+Z,out} - q_{-Z,out} \tag{57}$$

In the case of Rosetta, the SAPs are always pointing normal to the Sun, and the components along the X and Z directions can be expressed in terms of the unit vectors along the mechanical frame. Thus, by substituting Eqs. (55)–(57) into Eq. (54), the acceleration components induced by the TRP on each of the relevant surfaces can be written as

$$\mathbf{a}_{TRP,SAP} = -\frac{2}{3}\frac{q_{net,SAP}}{mc}A_{SAP}\mathbf{s} \tag{58}$$

$$\mathbf{a}_{TRP,X} = -\frac{2}{3}\frac{q_{net,X}}{mc}A_X\mathbf{x}_m \tag{59}$$

$$\mathbf{a}_{TRP,Z} = -\frac{2}{3}\frac{q_{net,Z}}{mc}A_Z\mathbf{z}_m \tag{60}$$

5. Results and discussions

5.1. Calculation conditions

When applying the analytical model previously established, we use the following data as inputs for the calculations.

- Orbit state
- Attitude state
- HGA pointing model
- Temperature measurements on SAPs
- Spacecraft mass history

From the orbit and attitude state knowledge, we can obtain the relative distance and angle of the Sun with respect to the spacecraft surfaces. In addition, the mean value of the temperature measurements on the two SAPs is taken as the best estimate of the temperature of the front side. Together with the resulting rear side temperature, we use these data for the calculations of the TRP acceleration components.

5.2. HGA contributions

The SAPs orientations are always kept pointing normal to the Sun direction and are the major contributors to the total SRP acceleration. Therefore, Figs. 20–24 provide the absolute value of the total acceleration components along the Sun vector for the five cruise phases. This includes the contributions by the SAPs, the $+X$ and $+Z$ sides, and with/without HGA's.

There are conspicuous spikes in the curves for both the "with HGA" and the "without HGA" cases, e.g. the spikes in the second half of cruise 1. These spikes are due to spacecraft attitude changes as discussed below Fig. 10. For example in the second half of cruise 1, the Sun elevation

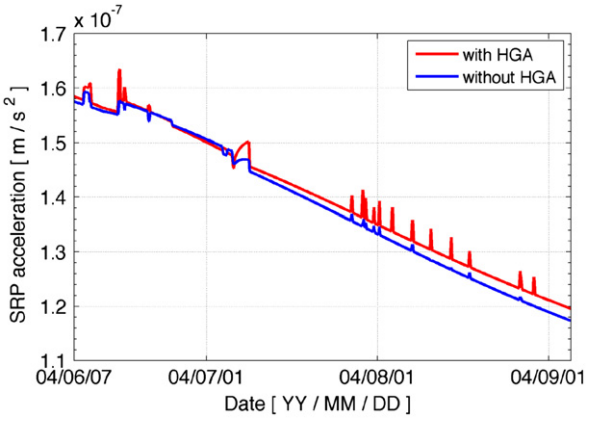

Fig. 20. SRP acceleration component along Sun vector with/without HGA in cruise 1.

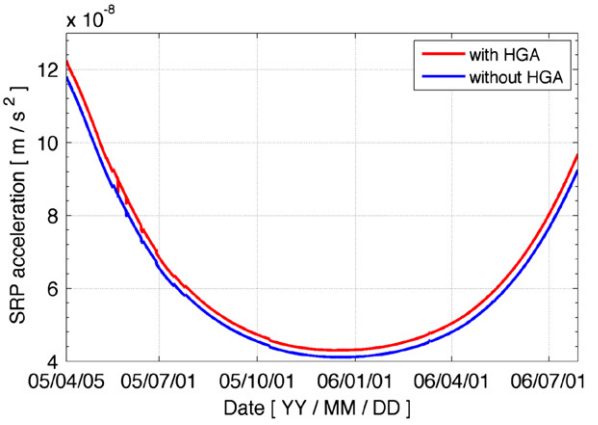

Fig. 21. SRP acceleration component along Sun vector with/without HGA in cruise 2.

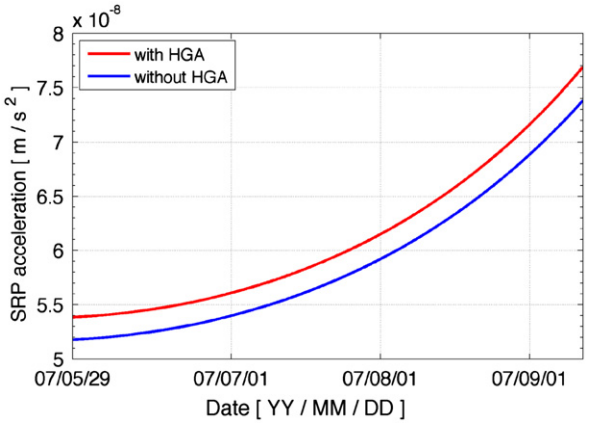

Fig. 22. SRP acceleration component along Sun vector with/without HGA in cruise 3.

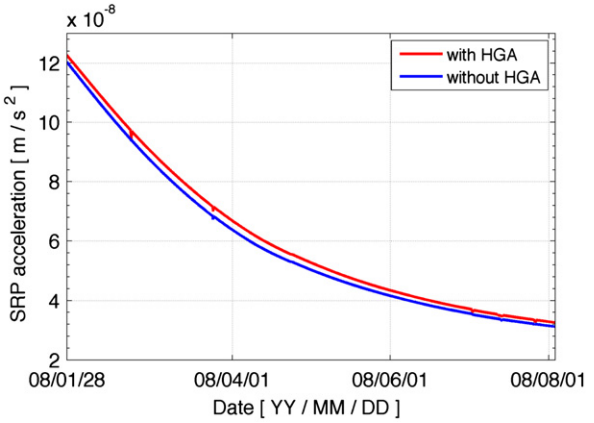

Fig. 23. SRP acceleration component along Sun vector with/without HGA in cruise 4.

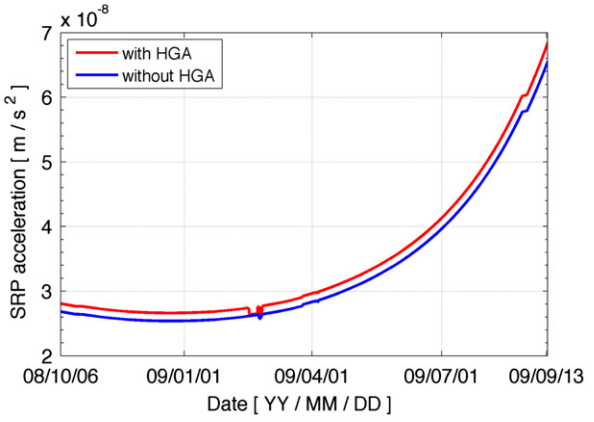

Fig. 24. SRP acceleration component along Sun vector with/without HGA in cruise 5.

increases up to 60° at each spike while the HGA is kept at 90° elevation. Physically, this attitude motion reduces the angle between the incident Sun and the HGA pointing axis h_1. Therefore, the HGA contribution along the Sun direction increases at each spike. In addition, it is because of the differences in the $+X$ and $+Z$ body surface areas are responsible for the small spikes in the "without HGA" data are induced.

The following Figs. 25–29 show the HGA contributions expressed in terms of percentages of the SRP accelerations along **s**, for the respective cruise phases. The average of

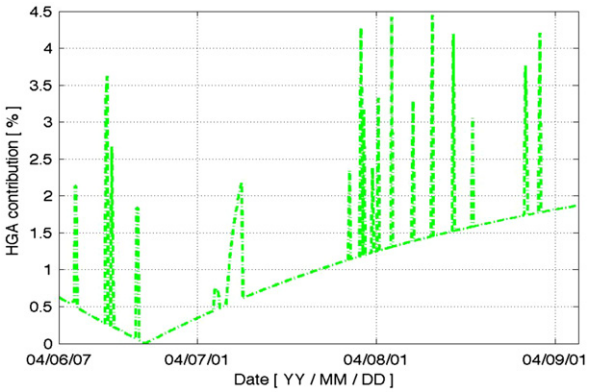

Fig. 25. HGA contributions as percentages of the SRP acceleration in cruise 1.

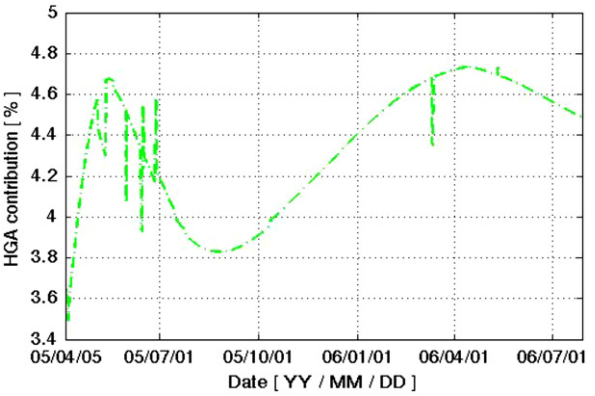

Fig. 26. HGA contributions as percentages of the SRP acceleration in cruise 2.

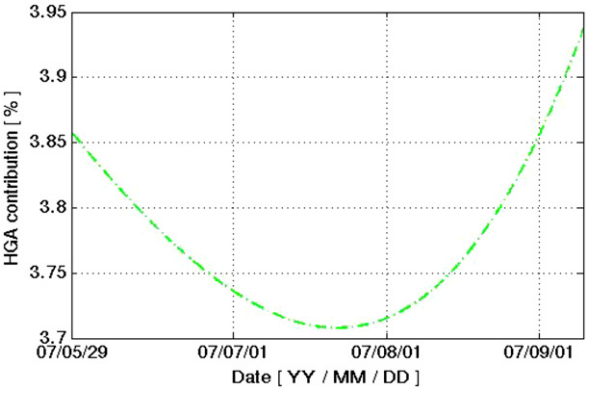

Fig. 27. HGA contributions as percentages of the SRP acceleration in cruise 3.

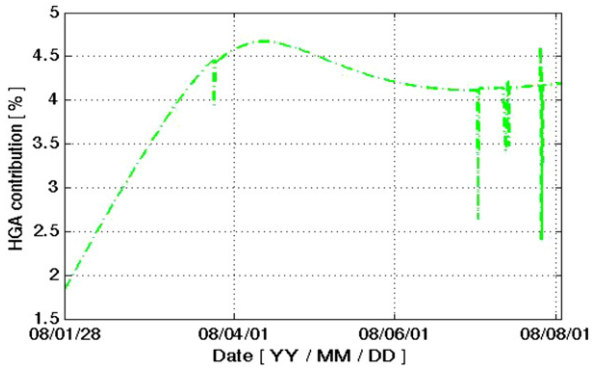

Fig. 28. HGA contributions as percentages of the SRP acceleration in cruise 4.

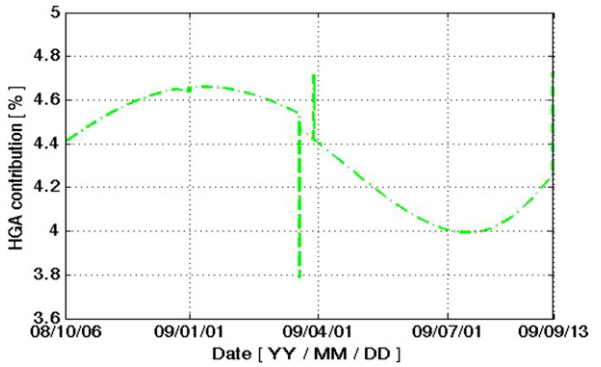

Fig. 29. HGA contributions as percentages of the SRP acceleration in cruise 5.

Table 5
HGA contributions with respect to SRP acceleration along Sun direction.

Phase	Min. [%]	Ave. [%]	Max. [%]
Cruise 1	0.00	0.91	2.19
Cruise 2	3.49	4.33	4.74
Cruise 3	3.71	3.77	3.96
Cruise 4	1.85	3.99	4.67
Cruise 5	3.79	4.30	4.72

these HGA contributions over each phase are summarized in Table 5.

Since the HGA pointing axis is kept almost normal to the Sun throughout the cruise 1, the contribution of the HGA is close to 0. Vice versa, in the other cruise phases, the elevation differences of the Sun and HGA are mostly in the range from 20 to 50 degrees. Thus, the SRP accelerations exerted on the HGA have larger contributions in average for these phases.

5.3. Model validation

Finally, Figs. 30–34 show comparisons of the established results and the SRP accelerations calculated by ESOC's orbit determination (OD) software. The calculated accelerations are publicly available via ESOC's TASC

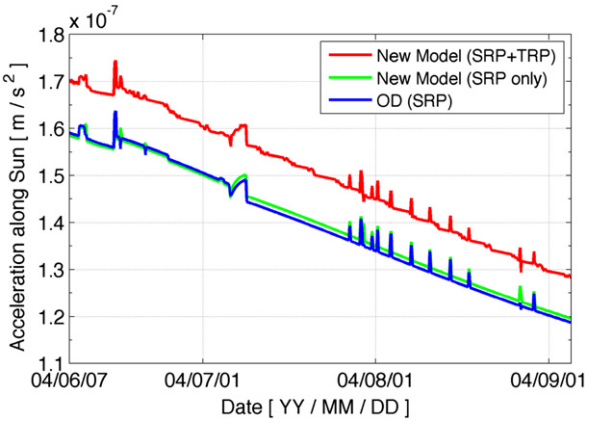

Fig. 30. Acceleration components of established models and operational OD data along Sun vector in cruise 1. (For interpretation of the references to colour in this figure, the reader is referred to the web version of this article.)

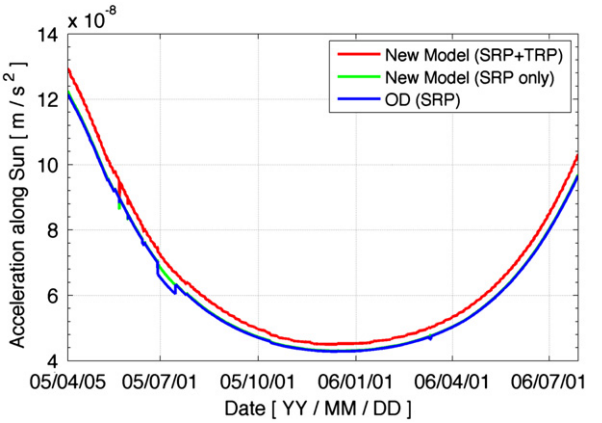

Fig. 31. Acceleration components of established models and operational OD data along Sun vector in cruise 2. (For interpretation of the references to colour in this figure, the reader is referred to the web version of this article.)

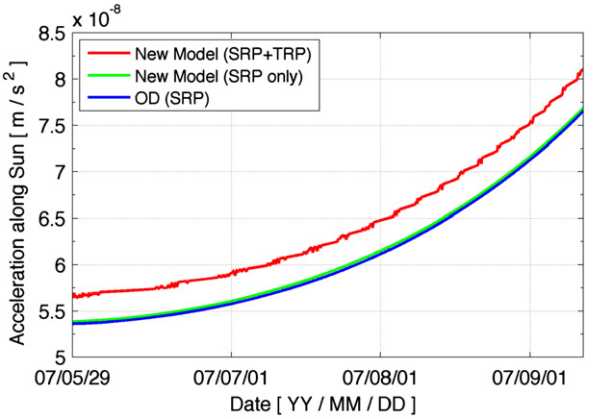

Fig. 32. Acceleration components of established models and operational OD data along Sun vector in cruise 3. (For interpretation of the references to colour in this figure, the reader is referred to the web version of this article.)

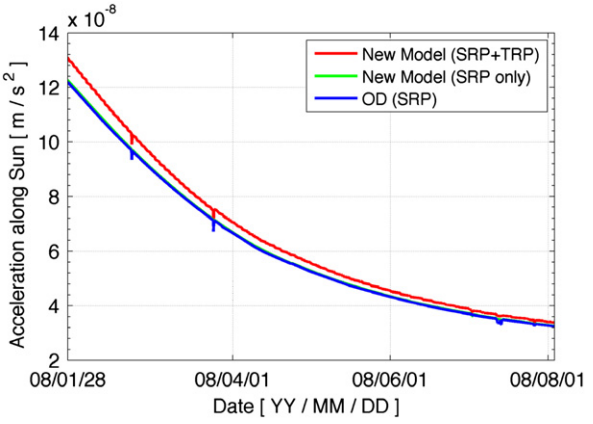

Fig. 33. Acceleration components of established models and operational OD data along Sun vector in cruise 4. (For interpretation of the references to colour in this figure, the reader is referred to the web version of this article.)

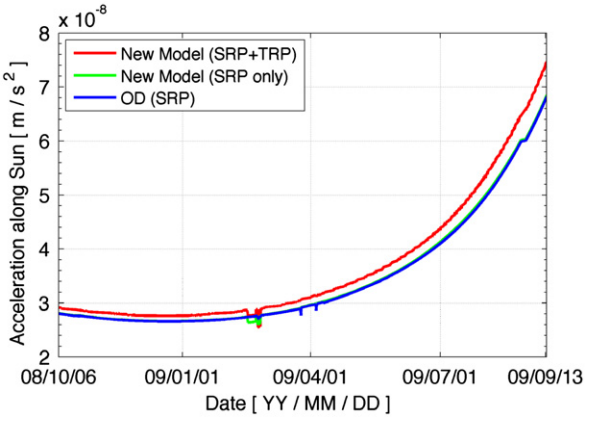

Fig. 34. Acceleration components of established models and operational OD data along Sun vector in cruise 5. (For interpretation of the references to colour in this figure, the reader is referred to the web version of this article.)

website together with the accessory software packages [8]. It is important to note that the SRP acceleration components have been extracted from the TSAC website (i.e. blue lines in Figs. 30–34). They do not include any scale factor corrections. Thus, it is of interest to compare the extracted accelerations from the TASC website with our established SRP model for validation.

The accelerations shown in Figs. 30–34 are the components along the Sun vector in $\boldsymbol{F}_m$. Each plot contains the SRP accelerations calculated by using ESOC software (blue lines), our established SRP model (green lines), and the total of our SRP and TRP models (red lines). Both of the SRP results include the effects on the SAPs, body surfaces, and HGA.

It is clear from Figs. 30–34 that our and ESOC's SRP results are essentially identical and that the effect of the TRP is significant. Table 6 summarizes the mean differences of the two SRP results and the TRP contributions with respect to the ESOC SRP accelerations for the respective cruise phases.

Table 6
SRP acceleration differences and TRP contributions with respect to OD results.

Phase	SRP difference (Average) [%]	TRP contribution		
		Min. [%]	Mean [%]	Max. [%]
Cruise 1	0.65	3.40	7.24	7.91
Cruise 2	0.48	4.24	5.57	6.71
Cruise 3	0.52	4.69	5.31	5.88
Cruise 4	0.49	3.45	5.10	6.96
Cruise 5	0.45	3.11	5.23	9.51

Table 6 shows that the differences between the two SRP results are well below 1% throughout all cruise phases. This correspondence confirms the validity of the established SRP model. Thus, the differences between the established model (red lines) and the SRP accelerations established by OD (blue lines) reveal the effective contribution of the TRP effects.

The TRP contributions in Table 6 are obtained from the TRP acceleration $\mathbf{a}_{TRP}$ and the SRP accelerations extracted from OD software $\mathbf{a}_{SRP,OD}$.

$$(TRP\ \ contribution) = \left|\frac{\mathbf{a}_{TRP}}{\mathbf{a}_{SRP,OD}}\right| \times 100 \tag{61}$$

The average of the TRP acceleration contribution ratio is within the range of 5.1–7.2% of the SRP accelerations established by the mission operations software. This result is consistent with the reported range of the observed errors during cruise phase operations [10].

From Table 6, the ratio of the TRP effect ranges up to 9.5% with respect to the SRP accelerations. In practice, the TRP effects may largely be accounted for by the scale factors introduced in the SRP model. However, because of the qualitative differences between the TRP and SRP effects, the scale factor approach has shortcomings. Therefore, we conclude that the (present) nominal SRP acceleration model in the OD software can be appreciably improved by including a TRP model.

It is difficult to quantify the orbit determination error in general since there are large variations in the trajectories and the relative geometries that influence the SRP and TRP effects as well as the orbit determination accuracy. Further insights on the actual orbit determination errors of Rosetta are provided in Ref. [10].

6. Conclusions

This paper establishes high fidelity analytical models for the accelerations due to the solar radiation pressure and thermal recoil pressure effects on ESA's Rosetta spacecraft. The model calculates the contributions by the solar array panels, the spacecraft body surfaces, and the high gain antenna through a straightforward step-by-step approach. The results show that the presented analytical model accurately describes the acceleration induced by the solar radiation pressure. The incorporation of the TRP model in the orbit determination software can lead to an appreciable improvement in the trajectory predictions of deep-space missions.

The thermal model presented here intends to enhance the orbit determination process of deep-space missions.

Acknowledgement

We acknowledge the contributions of Dr. Trevor Morley of ESA/ESOC by providing data and other valuable information on the Rosetta spacecraft and its operations.

References

[1] T. Morley, F. Budnik, ROSETTA Navigation at its First Earth Swing-by, in: Proceedings of the 25th International Symposium on Space Technology and Science, Kanazawa, Japan, June 4–11, 2006, Paper ISTS-2006-d-52.
[2] M. Terauchi, I. Kim, T. Hanada, J. C. van der Ha, Effect of Thermal Radiation Force for Trajectory during Swing-by, in: Proceedings of the 26th International Symposium on Space Technology and Science, Hamamatsu, Japan, June 2–6, 2008, Paper ISTS-2008-d-60.
[3] T. Morley, personal communication.
[4] J. Marshall, S.B. Luthcke, Modeling radiation forces acting on topex/poseidon for precision orbit determination, Journal of Spacecraft and Rockets 31 (1) (1994) 99–105 Jan–Feb.
[5] M. Ziebart, S. Adhya, A.J. Sibthorpe, S. Edwards, P.A. Cross, Combined radiation pressure and thermal modelling of complex satellites: algorithms and on-orbit tests, Advances in Space Research 36 (2005) 424–430.
[6] J.C. van der Ha, D. Stramaccioni, Thermal Radiation Effects on Deep-Space Trajectories, in: Proceedings of the AAS/AIAA Space Flight Mechanics Conference, San Diego, CA, USA, February 14–17, 2010, Paper AAS-10-226.
[7] Y. Sugimoto, J. C. van der Ha, B. Rievers, Thermal Radiation Model for Rosetta Spacecraft, in: Proceedings of the AIAA/AAS Astrodynamics Specialist Conference, Toronto, Ontario, Canada, August 2–5, 2010, Paper AIAA-2010-7659.
[8] ESOC Toolkit for Auxiliary Science Calculations (TASC) website, 〈http://tasc.esa.int/〉.
[9] Y. Mimasu, J. C. van der Ha, R. Funase, O. Mori, J. Kawaguchi, K. Shirakawa, Solar Radiation Pressure Model for Attitude Motion of Hayabusa in Return Cruising, in: Proceedings of the 60th International Astronautical Congress, Daejeon, S. Korea, October 12–16, 2009, Paper IAC-09.C1.9.9.
[10] M. A. Shoemaker, J. C. van der Ha, T. Morley, Reconstruction of Rosetta's Thermal Radiation Effects Using Orbit Determination Results, in: Proceedings of the AIAA/AAS Astrodynamics Specialist Conference, Toronto, Ontario, Canada, August 2–5, 2010, Paper AIAA-2010-8263.